Rayleigh-Bénard convection in binary mixtures with separation ratios near zero

Marco A. Dominguez-Lerma, Guenter Ahlers, and David S. Cannell
Department of Physics and Center for Nonlinear Science, University of California, Santa Barbara, California 93106
(Received 5 June 1995)

We present an experimental study of convection in binary mixtures with separation ratios Ψ close to zero. Measurements of the Hopf frequency for $\Psi<0$ were used to determine the relationship between Ψ and the mass concentration x with high precision. These results are consistent with but more precise than earlier measurements by conventional techniques. For $\Psi>0$, we found that the pattern close to onset consisted of squares. Our data give the threshold of convection $r_c \equiv R_c/R_{c0}$ (R_c is the critical Rayleigh number of the mixture and R_{c0} that of the pure fluid) from measurements of the refractive-index power of the pattern as revealed by a very sensitive quantitative shadowgraph method. Over the range $\Psi \lesssim 0.011$, corresponding to $r_c \gtrsim 0.2$, these results are in good agreement with linear stability analysis. The measured refractive-index power varies by six orders of magnitude as a function of r and for $r \gtrsim 0.55$ is in reasonable agreement with predictions based on the ten-mode Lorenz-like Galerkin truncation of Müller and Lücke [H. W. Müller and M. Lücke, Phys. Rev. A **38**, 2965 (1988)]. For smaller r, the model predicts a cancellation between contributions to the refractive index from concentration and temperature variations, which does not seem to occur in the physical system. Determinations of the wave numbers of the patterns near onset are consistent with the theoretically predicted small critical wave numbers at positive Ψ. As r approaches one, we find that q approaches the critical wave number $q_{c0} \simeq 3$ of the pure fluid.

PACS number(s): 47.20.Bp, 47.54.+r, 47.20.Ky, 47.27.Te

I. INTRODUCTION

Convection in a thin horizontal layer of a single-component fluid heated from below, known as Rayleigh-Bénard convection [1], has long been used as one of the model systems for the study of pattern formation. The phenomena that are observed depend on an external control parameter

$$R \equiv \frac{\beta_1 g d^3 \Delta T}{\kappa \nu} , \tag{1.1}$$

which is known as the Rayleigh number. Here β_1 is the isobaric thermal expansion coefficient, g the acceleration of gravity, d the thickness of the fluid layer, κ the thermal diffusivity, and ν the kinematic viscosity. R can readily be changed in an experiment by changing the applied temperature difference ΔT. Increasing R will increase the destabilizing density gradient associated with the temperature gradient, since the less (more) dense fluid will be located at the bottom (top) of the sample. Convection will first occur when R exceeds a critical value $R_{c0}=1708$, and for larger R various flow patterns will evolve. Precisely what occurs depends also on the Prandtl number

$$\sigma \equiv \nu/\kappa , \tag{1.2}$$

which is a property of the fluid and is thus not as readily adjusted in a given experiment. An impression of the diversity of the phenomena that are encountered can easily be obtained by a glance at some of the recent literature [2–10].

Convection in binary mixtures can reveal numerous additional pattern-formation phenomena that do not occur in pure fluids [11]. In this system, there are two contributions to the density gradient. One of them comes from the ordinary thermal expansion of the fluid at constant pressure P and mass concentration x, as quantified by the expansion coefficient

$$\beta_1 \equiv -(1/\rho)(\partial\rho/\partial T)_{P,x} . \tag{1.3a}$$

When heating is from below, this contribution is destabilizing when $\beta_1>0$, which is the usual case. The other contribution is due to the density variation resulting from the concentration gradient, which is induced by the imposed temperature gradient. Its magnitude depends on the solutal expansion coefficient

$$\beta_2 \equiv -(1/\rho)(\partial\rho/\partial x)_{P,T} , \tag{1.3b}$$

as well as on the Soret coefficient S_T, and it can be stabilizing or destabilizing, depending on the particular mixture that is used. The net effect of the concentration gradient on the stability of the system is described by the separation ratio

$$\Psi \equiv -\frac{\beta_2}{\beta_1} x(1-x) S_T . \tag{1.4}$$

The value of Ψ depends on the particular fluid mixture and can be positive or negative. It can be varied over a wide range [12] by simply changing the concentration. When $\Psi<0$, the induced concentration gradient is stabilizing and in part counteracts the destabilizing density gradient due to β_1. In that case, the threshold is elevated, i.e., $R_c > R_{c0}=1708$. It is possible for the concentration gradient to temporally lag behind the thermal gradient,

leading to oscillations. This interesting phenomenon is responsible for the existence of traveling waves and much of what has been studied in binary mixtures over the past decade [11]. On the other hand, when $\Psi > 0$, both the concentration gradient and the thermally induced density gradient are destabilizing and the Soret effect leads to a lowered threshold for the onset of convection, i.e., to $R_c < R_{c0} = 1708$. The pattern at onset is then expected to be time independent. Although there have been some early experiments in this parameter range [13–16] this case has had far less attention than the one with $\Psi < 0$. The present paper deals primarily with mixtures that have positive ψ.

It turns out that there are good reasons why the range of positive Ψ has been relatively neglected by experimentalists. First, it is fair to say that the variety of phenomena that occur is not as great as it is for negative Ψ, although a number of interesting effects are expected nonetheless. One of them is that, on the basis of linear stability analysis, the characteristic wave number of the pattern at onset is expected to become small as Ψ increases above zero [17–22]. In the ideal laterally infinite system with rigid, impermeable boundaries, the wave number at onset is predicted to vanish at [19,21,23]

$$\Psi_0 = \mathcal{L}/(\tfrac{34}{131} - \mathcal{L}) \tag{1.5a}$$

and [17,21]

$$R_c(\Psi_0) = 6\mathcal{L}/\Psi_0 \ . \tag{1.5b}$$

Here

$$\mathcal{L} \equiv D/\kappa \sim 10^{-2} \tag{1.6}$$

is the Lewis number and D is the mass diffusivity. Wave numbers smaller than those characteristic of convection in a pure fluid near onset have been observed in previous experiments at positive Ψ [14–16] albeit only well above the actual bifurcation where the prediction mentioned above really does not apply and where the choice of a particular wave number is a wave-number-selection problem that is essentially unsolved theoretically. Another interesting effect is that, for $\Psi < \Psi_0$, the pattern immediately above onset is predicted to be one of squares [21,24]. This prediction is consistent with experimental evidence [14–16,25] and numerical calculations [26] well above the onset of convection, but prior to the present work there was no direct experimental determination of the flow pattern close to the bifurcation point. The occurrence of squares can quite generally be attributed to the impermeability of the boundaries to one of the fluxes [14,21], in this case the concentration flux. Similarly, squares occur in convection of a simple fluid when the boundaries are insulating, i.e., impermeable to the heat flux [27–30]. In the present paper we will present measurements of the wave number relatively close to onset and determinations of the pattern immediately above onset, which agree with the theoretical predictions.

The other reason for the relative scarcity of experimental information is the great difficulty of making quantitative or even qualitative measurements close to onset when Ψ is positive. The problem is associated with the fact that, in liquid mixtures, the time scale of mass diffusion is longer by two orders of magnitude than that of heat diffusion. This is quantified by $\mathcal{L}$, which is equal to the ratio of these two time scales. An obvious consequence is that the establishment of a steady state can take a very long time. However, more serious is the fact that, even in steady state, the small $\mathcal{L}$ leads to *extremely* feeble, nearly undetectable, convective flows in the so-called "Soret regime" between R_c and R_{c0}. There the flow is driven primarily by the concentration gradients. Since these are established very slowly and since any hydrodynamic flow tends to eliminate them, the induced velocities are very small indeed even well above threshold. This situation changes quickly when R passes R_{c0}, where the usual Rayleigh-Bénard mechanism is operative. In this "Rayleigh regime" patterns are easily discernable, for instance, by standard shadowgraph methods and the heat transport associated with the convection is readily measured. For R significantly below R_{c0}, however, the hydrodynamic contribution to the heat transport cannot be measured by known experimental techniques and the patterns heretofore had not been determined.

In the present work we refined the shadowgraph technique to the point where we could detect patterns involving relative variations in the refractive index that were smaller than one part in 10^9. This enabled us to detect and measure the amplitude of patterns immediately above the Soret onset at R_c over the range $0 \lesssim \Psi \lesssim 0.011$. As Ψ increased, we used thinner cells so as to maintain a reasonable value for ΔT_c as the critical Rayleigh number decreased. Our results for R_c agree with linear stability analysis. In our parameter range we found that squares are the stable planform near onset. Also consistent with linear theory, we measured a wave number near onset that is smaller than that for a pure fluid.

II. EXPERIMENTAL APPARATUS AND METHOD

The apparatus is shown schematically in Fig. 1. The lower portion depicts the cylindrical container that accommodated the cell in its central region. The upper portion shows the optical shadowgraph system that was used to visualize the flow.

Temperature-controlled water was circulated axisymmetrically in the container, as indicated by the arrows in the figure. It entered from below and was diverted around a cylindrical can that enclosed the cell. It then passed through the flow distributor, a hollow donutlike ring that was built to deliver the water symmetrically onto the cell's top surface by means of 32 thin grooves machined into its lower surface. For most of the experiments at positive Ψ we used, in addition to the grooves, a set of turrets on top of the flow distributor to redirect the flow down to the center of the cell as shown. However, these turrets turned out to be responsible for a small *increase* in the radial gradient of the cell's top temperature and were eliminated in the experiments carried out at negative Ψ. The water was recirculated close to the lateral wall of the container, thus providing overall protection against temperature fluctuations of the laboratory.

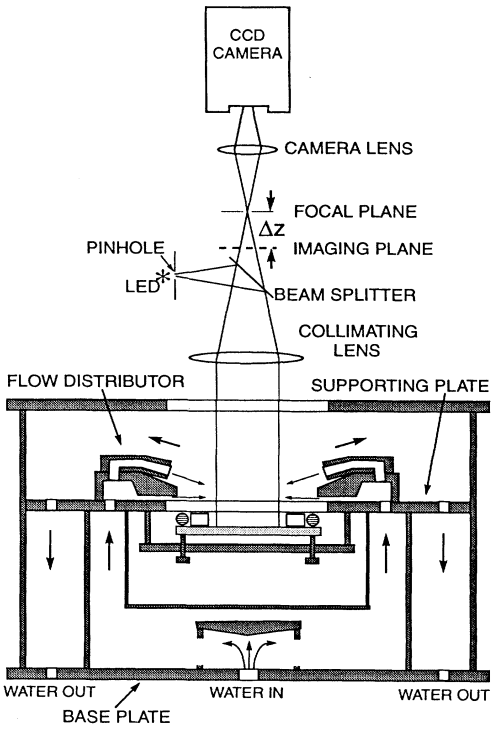

FIG. 1. Schematic drawing of the apparatus.

This apparatus is similar to one described elsewhere [31], except that its lateral size is somewhat larger and that it is constructed primarily from stainless steel instead of aluminum.

In order to assess how constant and symmetric the temperature was at the top surface of the sapphire plate, we translated a small thermistor mounted in a glass tube across that surface. Although the temperature distribution was azimuthally symmetric within about 1 mK, there was a radial gradient of about 4 mK/cm with the turrets in place and about 1 mK/cm without them when the vertical temperature difference across the cell was 3.5 °C. Because of the high conductivity of sapphire, the temperature at the top of the sample (bottom of the sapphire) was somewhat more uniform.

We used three cylindrical cells. Their top and bottom surfaces were formed by an optically flat sapphire and a silver plate that had diameters of 10.16 and 8.89 cm and were 0.953 and 0.71 cm thick, respectively. These materials were chosen because of their large thermal conductivities as compared to those of the fluid mixtures. The silver-plate surface that was in contact with the mixture was diamond machined to serve as a mirror for the shadowgraph. Its other flat surface had a metal-film heater glued to it.

A high-density polyethylene (HDPE) ring sandwiched between the two plates defined the fluid layer's lateral boundary. A Viton O ring, stretched around the HDPE ring, was used to seal the cell. Sealing was done by pushing the silver plate from below by means of six screws evenly spaced on a circle directly below the O ring. We built cells with heights of $d = 0.329$, 0.240, and 0.160 cm, diameters of 6.94, 6.35, and 6.94 cm, and thus radial aspect ratios of 10.6, 13.2, and 21.8, respectively. They will be referred to as cells 1, 2, and 3, respectively. The thinner cells made the shadowgraph method more sensitive (see Sec. III A below) and allowed us to visualize very weak flows at the larger values of Ψ. As determined by interferometry, the cell heights were constant to better than ± 1 μm over the circular area occupied by the fluid layer.

HDPE was used for the cell's lateral boundary for two reasons. First, it is quite impermeable to ethanol and water as compared with other plastics. This impermeability helped to maintain the concentration of the mixture constant in time. Second, HDPE has a thermal conductivity that is very close to those of the fluid mixtures that we used. This similarity helped to reduce the horizontal gradient caused by the sapphire's finite thermal conductivity and the mismatch of conductivities between the cell wall and the mixture [32,33]. We carried out steady-state two-dimensional simulations of the temperature profiles of the cells [7] to estimate the magnitude of the radial gradient. The heat-conduction equation was integrated for the rectangular vertical cross section of the cell, which is illustrated in the top portion of Fig. 2. There the top and the bottom boundaries were set to a constant temperature and the lateral boundaries were considered to be adiabatic. The top and the bottom boundaries simulated the sapphire's and silver's top surfaces, respectively. One of the lateral boundaries was located at the center of the cell while the other was at the sapphire's edge. In units of the sample conductivity, we used 86.7, 0.062, 0.72, and 1.18 for the conductivities of the sapphire, the air, the O ring, and the HDPE, respectively.

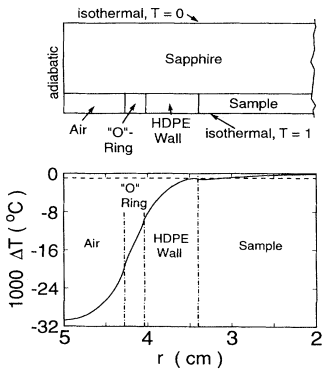

FIG. 2. Calculated temperature variation along the sample-sapphire interface. The top diagram is a schematic drawing of the approximation of the cell cross section for which the simulation was carried out. The temperature at the top of the sapphire was set to zero and the temperature at the top surface of the silver bottom plate was set to one. The bottom figure gives the temperature deviation ΔT from the temperature at the sample-sapphire interface at the cell center. The horizontal dashed line indicates a temperature perturbation equal to 0.1% of the total temperature difference across the cell.

We found that by increasing the width of the HDPE ring we could decrease the magnitude of the radial gradient substantially. Without compromising the aspect ratio excessively, we designed the three cells so that the radial change in temperature at the sapphire's bottom surface from the center of the fluid layer to the HDPE inner lateral edge was only about 1 mK when the vertical temperature difference was 1 K. In the bottom part of Fig. 2 we show the radial variation of the temperature at the sapphire-sample boundary for cell 2.

We prepared 2 kg each of several mixtures by weight with mass fractions x such that the associated values of Ψ were close to zero. Distilled, deionized water and high-purity ethanol were used. The concentration was known within one or two parts in 10^4. About 400 cm^3 of the solution was quickly transferred into a heavy-walled Erlenmeyer flask, where it was frozen using liquid nitrogen. The flask was then evacuated for 10 sec to remove desorbed gases and thawed. This freeze-and-thaw degassing procedure was repeated twice. It was found that this was adequate to prevent the formation of bubbles at a later time in the convection cell. About 50 cm^3 of the degassed mixture was withdrawn with a syringe and slowly injected into the sample cell via one of two thin Teflon tubes that were snuggly inserted into two holes 180° apart at midheight through both the O ring and the HDPE ring. We expect that the total uncertainty in the concentrations, including that due to preferential evaporation and other effects, does not exceed ± 0.0005. The concentrations and other properties of the mixtures that we used are listed in Table I. We obtained the density and its derivatives from Ref. [34], the viscosity from Ref. [35], and the thermal and mass diffusivity from Ref. [12].

The upper part of Fig. 1 shows the optical components of the shadowgraph apparatus that was used to visualize the flow patterns. Those components were accommodated in a tall aluminum tube, 135 cm long and 14 cm in diameter, which was attached concentrically to the cover plate of the cylindrical container. The tube consisted of two shorter sections of roughly equal length that were screwed together. The bottom tube contained the light source, a beam splitter in the form of a thin pellicle, and a high-quality collimating lens with a focal length of 64 cm. These parts were used, first, to produce a parallel beam along the axis of the cylindrical cell and, second, to collect the beam that was reflected from the bottom of the cell, which had been modified by the lateral index-of-refraction variations in the fluid.

The light source was a red (650-nm) light-emitting diode [36] (LED) behind a 45-μm-diam pinhole. The front surface of the LED's plastic enclosure from which the beam emerged was machined flat at a plane that was very close to the glowing semiconducting region. The pinhole was glued to the surface above the emitting region, but in a location that avoided the lead. This pseudo-point-source was positioned at the focal point of the collimating lens as viewed by the beam splitter. After reflection of the light beam from the bottom plate, the image of the source was centered in a small circular hole 0.1 cm in diameter lying in the focal plane of the collimating lens above the beam splitter. This aperture served as a spatial filter to eliminate the light reflected from various glass-sapphire-fluid-air interfaces in the apparatus, which were inclined at small angles relative to the bottom plate. The light passing through this hole reached the camera system located inside the top tube.

The camera system consisted of a black and white charge coupled device (CCD) camera (Sony model SSC-M354) and a 50-mm focal length $f/1.4$ Nikon camera lens, both of which could be translated independently along the common axis of the top and bottom tubes. The distance between the camera and the lens was adjusted to

TABLE I. Parameters of the experimental runs in cells 1, 2, and 3 (see Table III below). Column 2 gives the mass fraction x of ethanol for each mixture. These values are subject to errors of ± 0.0005. The third column gives the mean temperature with $\Delta T = \Delta T_c$. The fourth, fifth, and sixth columns give the Prandtl number σ, Lewis number $\mathcal{L}$, and separation ratio Ψ. Here σ and $\mathcal{L}$ are based on Refs. [12] and [35] and Ψ was determined from Eqs. (5.1) and the values of x. The measured (dimensionless) Hopf frequency for $\Psi < 0$ is given in column 7. Columns 8 and 9 give ΔT at the onset of Rayleigh (ΔT_{c0}) and of Soret (ΔT_c) convection, respectively.

Cell	x	$\bar{T}$ (°C)	σ	$10^3\mathcal{L}$	$10^2\Psi$	ω	ΔT_{c0} (°C)	ΔT_c (°C)
2	0.280	28.32	20.3	8.3	−1.45	2.40	3.87	
2	0.280	32.35	17.8	9.5	−1.25	2.23	3.26	
2	0.284	28.29	20.5	8.0	−0.73	1.62	3.82	
2	0.284	32.34	18.0	9.1	−0.62	1.37	3.23	
2	0.286	28.27	20.6	7.8	−0.37	1.33	3.80	
2	0.286	32.33	18.1	8.9	−0.31	1.21	3.22	
2	0.287	28.25	20.6	7.8	−0.19	0.87	3.78	
2	0.287	32.31	18.9	8.7	−0.15	0.72	3.20	
2	0.288	27.80	20.6	7.7	−0.01		3.82	3.38
2	0.290	27.15	21.4	7.3	0.35		3.80	2.09
2	0.292	26.90	21.6	7.1	0.72		3.79	1.59
1	0.292	26.44	21.6	7.1	0.73		1.57	0.66
2	0.294	26.86	21.7	7.0	1.09		3.77	1.51
3	0.294	27.60	18.8	8.1	1.07		10.8	2.90

set the magnification of the image. The camera-lens system was translated jointly so as to image a plane (see Fig. 1) located a distance Δz below the focal point of the collimating lens onto the CCD element. Thus the spatial distribution of the light intensity in that plane could be measured.

III. DATA ANALYSIS

A. Analysis of the shadowgraph measurements

The shadowgraph technique [32,37,38] used to visualize the convective flow patterns provides a signal related to the vertical average of the lateral refractive-index variation in the cell and thus the images are the net result of contributions from lateral temperature and concentration variations. As indicated in Fig. 1, the light beam passed twice vertically through the cell, being reflected by the bottom plate. The signal was generated by imaging a plane a distance Δz below the focal plane of the collimating lens onto the CCD element at the camera. This is equivalent to viewing the shadowgraph signal, which, in the absence of the collimating lens, would have formed at an optical distance

$$z_1 = z_0 + \frac{f(f-\Delta z)}{\Delta z} \tag{3.1}$$

from the cell. Here $z_0 \simeq 18$ cm is the optical distance from the sample to the collimating lens, including corrections for the refractive indices of the water and windows in the optical path. For the present experiments, Δz was 3.99 cm, giving $z_1 = 980$ cm.

We took images containing $m_0 = 256 \times 256 = 65\,536$ pixels and covering the entire circular cell. The light intensity at each pixel location was digitized so as to be described by 1 byte. A background image $\tilde{I}_0(\mathbf{x})$ was taken at a value of ΔT well below the critical value ΔT_c for the onset of convection ($\mathbf{x}$ is the horizontal position vector within the cell). Then ΔT was increased above ΔT_c and an image $\tilde{I}(\mathbf{x},r)$ was taken at each of many values of

$$r \equiv R/R_{c0} .$$

Typically, before each image at a new r value the system was permitted to equilibrate for about 2 h. The shadowgraph signal is defined to be

$$I(\mathbf{x},r) = [\tilde{I}(\mathbf{x},r) - \tilde{I}_0(\mathbf{x})]/\tilde{I}_0(\mathbf{x}) , \tag{3.2}$$

where the division on the right-hand side corresponds to pixel-by-pixel division of the image matrices. Two gray-scale images of $I(\mathbf{x},r)$, one each for $r = 1.05$ and 0.68, both for $\Psi = 0.0073$ ($x = 0.292$), are shown in Figs. 3(a) and 3(d).

In order to reduce effects associated with the sidewall and to obtain a quantitative measure of the flow amplitudes, the signal was processed further. We chose an origin at the cell center and computed the mean and the variance P of the part inside a diameter equal to 85% of the original image width, which included $m = 36\,621$ pixels. Pixel values outside this region were set equal to zero and the mean was subtracted from the pixel values within it. Gray-scale images of the results are shown in Figs. 3(b) and 3(e). To further reduce the contribution from experimental noise to the analysis of the shadowgraph signal, we worked in Fourier space. The images were Fourier transformed and the transform was normalized by dividing the real and imaginary parts by $(m_0 m)^{1/2} = 48\,990$. This normalization ensured that the total power in the Fourier transform was equal to the variance P of the selected central area of the original image (i.e., Parseval's theorem [39] still holds). For the examples from cell 1 given in Figs. 3(b) and 3(e) we obtained $P = 0.217$ and 1.15×10^{-4}, respectively (see the first row of Table II). Gray-scale images of the center $\frac{1}{4} \times \frac{1}{4}$ portions of the structure factors $S(\mathbf{q},r)$ (the square of the modulus of the Fourier transform) of the images in Figs. 3(b) and 3(e) are shown in Figs. 3(c) and 3(f).

We considered two methods of analysis of the structure factor. First we computed an azimuthal sum $S(q,r)$ of $S(\mathbf{q},r)$. Examples for $r = 1.05$ [Fig. 3(b)], 0.76, and 0.59 are shown in Fig. 4. The main peaks are quite narrow and we summed the four q values located closest to the

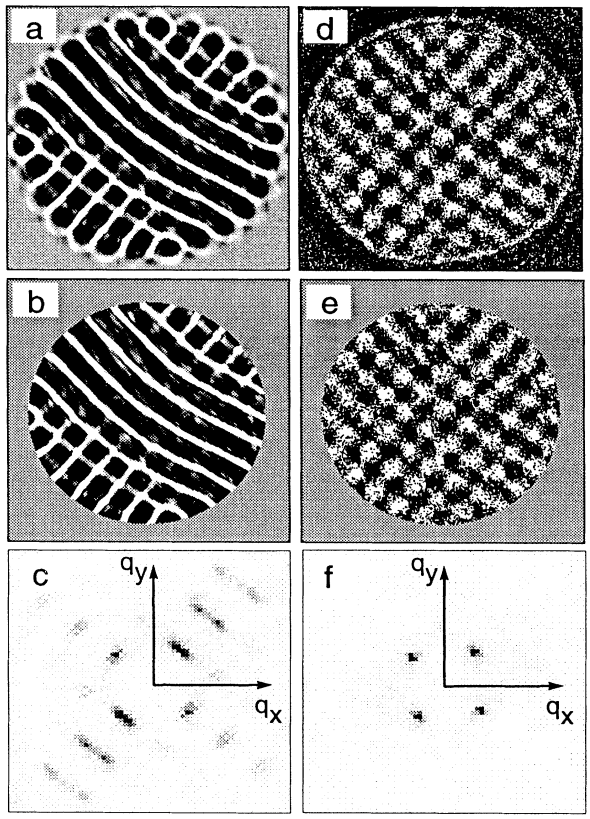

FIG. 3. Gray-scale images of convection patterns from cell 1 for $\Psi = 0.0073$ ($x = 0.292$). (a) and (d) are images of the entire cell for $r = 1.05$ and 0.68, respectively. (b)and (e) are the portions used in the Fourier analysis. (c) and (f) are the corresponding gray-scale representations of the center $\frac{1}{4} \times \frac{1}{4}$ portions of the structure factors of the images in (b) and (e).

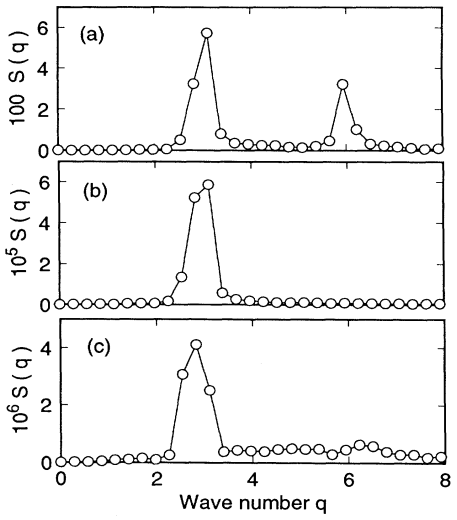

FIG. 4. Azimuthal sums of the structure factors of the images for cell 1 taken at $\Psi=0.0073$ ($x=0.292$) and (a) $r=1.05$, (b) $r=0.76$, and (c) $r=0.59$.

largest peak near $q\simeq 3$ to get estimates of the power P_r under the peak. A few examples are given in Table II. Comparing P_r with P, one sees that, at $r=1.05$, about half the power is located in the fundamental peak. The remainder is contained primarily in higher harmonics, which are caused primarily by nonlinearities of the shadowgraph method and saturation of the image-acquisition system. For $r=0.76$, P_r also corresponds to about half the total power (which is over three orders of magnitude smaller than for $r=1.05$), but in this case the remainder is due primarily to broadband instrumental noise originating in the camera. As r decreases further, the fraction of the power contained in the signal decreases also. At $r=0.59$ it is only about 12% of the total, but still measurable with good precision.

TABLE II. Results of several types of analyses of the structure factors. These examples are for cell 1 and $\Psi=0.0073$ (see the text for details).

r	1.05	0.76	0.68	0.59
P	0.217	2.18×10^{-4}	1.15×10^{-4}	8.2×10^{-5}
P_r	0.103	1.30×10^{-4}	4.0×10^{-5}	1.0×10^{-5}
$P_1^{(5)}$	0.070	6.2×10^{-5}	2.0×10^{-5}	4.8×10^{-6}
$P_2^{(5)}$	0.022	6.1×10^{-5}	1.8×10^{-5}	4.4×10^{-6}
$\theta_1^{(5)}$	51.1	140.3	51.5	51.5
$\theta_2^{(5)}$	140.7	51.8	140.2	140.5
$q_1^{(5)}$	2.97	2.92	2.86	2.80
$q_2^{(5)}$	3.02	2.90	2.88	2.79
$P_1^{(3)}$	0.047	5.7×10^{-5}	1.8×10^{-5}	4.2×10^{-6}
$P_2^{(3)}$		5.3×10^{-5}	1.6×10^{-5}	4.1×10^{-6}
$\theta_1^{(3)}$	49.0	140.3	52.0	51.7
$\theta_2^{(3)}$		52.4	140.3	140.6
$q_1^{(3)}$	2.98	2.92	2.84	2.79
$q_2^{(3)}$		2.89	2.88	2.80

The part of the instrumental noise with wave numbers close to the roll wave number will of course contribute to P_r. In order to reduce it further, we identified the locations of the two pairs of main peaks in $S(\mathbf{q},r)$ for each image [see Figs. 3(c) and 3(f)] and summed the 5×5 or 3×3 pixel values in their immediate vicinity to obtain the power estimates $P_i^{(5)}$ and $P_i^{(3)}$, respectively. The latter method also permitted a determination of the angles θ_1 and θ_2 [measured counterclockwise from the right-pointing horizontal axis labeled q_x in Figs. 3(c) and 3(f)] of the peak locations and the corresponding wave numbers q_1 and q_2. This determination was done by computing the first moment of $S(\mathbf{q},r)$ over the 5×5 or 3×3 pixels. Some examples are again given in Table II. It is apparent that the sum $P_1^{(i)}+P_2^{(i)}$ accounts for most of the power P_r, except in the case of the image in Fig. 3(c), where $P_i^{(3)}$ obviously missed a portion of the broadened peak. For well equilibrated square patterns throughout the Soret regime, we found $P_1^{(3)}+P_2^{(3)}$ to be an excellent estimate of the total power in the signal of interest. After subtracting a background determined below the onset of convection, we used it for the results given in Sec. VI.

The data in Table II also show that the angle $|\theta_2-\theta_1|$ between the two wave vectors is very close to 90°. Within experimental error the two wave numbers q_1 and q_2 are equal to each other. In the Soret regime, P_1 and P_2 are about equal. We conclude that the patterns quantitatively correspond to squares rather than to rhombi such as those observed in chemical patterns and in convection in nematic liquid crystals [40–43].

B. Relation to the refractive index

For a sufficiently weak convection pattern that causes a refractive-index deviation

$$\delta n(\mathbf{x},z,r)=\delta n(\mathbf{x},r)f(z) \tag{3.3}$$

within the fluid mixture, the linear shadowgraph signal $I(\mathbf{x},r)$ is related to δn by [37,38,44]

$$I(\mathbf{x},r)=-\mathcal{A}\langle f(z)\rangle_z\nabla^2\delta n(\mathbf{x},r)\ . \tag{3.4}$$

Here $\langle\ \rangle_z$ denotes an average over z. The function $f(z)$ in Eq. (3.3) may be chosen so that $\langle f(z)\rangle_z=1$. For a superposition of spatially periodic refractive-index variations of uniform wave number q, the signal then is

$$I(\mathbf{x},r)=\mathcal{A}q^2\delta n(\mathbf{x},r)\ . \tag{3.5}$$

For our experimental setup of a nearly parallel beam passing twice vertically through the cell,

$$\mathcal{A}=2d\gamma(z_1)z_1\ , \tag{3.6}$$

where d is the cell thickness, $\gamma(z_1)$ is a factor less than unity, which may be calculated on the basis of physical optics [38], and z_1 is the viewing distance given by Eq. (3.1). Table III gives values of $\mathcal{A}q^2$ and γ together with some of the other relevant parameters for each cell.

TABLE III. Parameters for the three cells. $\mathcal{A}$ was computed for $z_1=980$ cm and $q=\pi/d$. The onset of Rayleigh convection at ΔT_{c0} is for $x=0.292$ (the value for cell 3 is estimated). Values for s_θ and s_c are for $x=0.292$ and $T=27$ °C.

Parameter	Cell 1	2	3
d (cm)	0.329	0.240	0.160
γ	0.952	0.857	0.448
$10^{-4}\mathcal{A}q^2$	5.60	6.91	5.42
ΔT_{c0} (K)	1.57	3.79	(12.8)
$10^3 s_\theta$ (K)	0.919	2.23	7.49
$10^6 s_c$	3.28	7.92	26.7

Knowing $\mathcal{A}q^2$, Eq. (3.5) gives the vertical average of the refractive-index variation $\delta n(\mathbf{x},r)$, which may be compared with the prediction of a theoretical model.

IV. PREDICTIONS OF THE TEN-MODE MODEL

A. Solution of the model and relation to physical variables

The nonlinear properties of convection in binary mixtures with positive separation ratios were considered by Müller and Lücke (ML) [45]. These authors derived a Lorenz-like model based on a Galerkin truncation, which retained the amplitudes of ten modes and could represent a pattern of either straight rolls or of squares. The model incorporates physically realistic impermeable boundaries, but retains unrealistic slip boundary conditions at the top and bottom of the sample. It was evaluated for the assumption that the wave number q of the modes is equal to the critical wave number q_{c0} for $\Psi=0$, whereas in the physical system the wave number depends on the Rayleigh number and near onset is smaller than q_{c0}. Because of the boundary conditions and the choice for q, we expect at best semiquantitative agreement with experiment even if the mode truncation is adequate.

We are concerned only with the stationary states, i.e., with the fixed points of the model and not with the time dependence of the modes. ML treat the problem in terms of two scalar fields $\theta(\mathbf{x},z)$ and $\zeta(\mathbf{x},z)$, where $\mathbf{x}$ is the horizontal position vector (x,y) and z is the vertical coordinate (the use of x for position and concentration should not cause confusion because the meaning is clear from context). Here θ is the deviation of the local temperature from the pure-conduction profile and

$$\zeta(\mathbf{x},z)=c(\mathbf{x},z)-\Psi\theta(\mathbf{x},z)\ , \tag{4.1}$$

with $c(\mathbf{x},z)$ the deviation of the mass-concentration field from its pure conduction profile. In the theory, θ was scaled by

$$s_\theta\equiv\frac{\kappa\nu}{\beta_1 g d^3}\ . \tag{4.2a}$$

Similarly, c was scaled by

$$s_c\equiv\frac{\kappa\nu}{\beta_2 g d^3}=s_\theta\beta_1/\beta_2\ , \tag{4.2b}$$

with β_1 and β_2 given by Eqs. (1.3a) and (1.3b). Thus, in physical units the temperature and concentration deviations from the conduction profiles are given by

$$\tilde{\theta}(\mathbf{x},z)=s_\theta\theta(\mathbf{x},z) \tag{4.3a}$$

and

$$\tilde{c}(\mathbf{x},z)=s_c c(\mathbf{x},z)\ . \tag{4.3b}$$

From Eq. (1.1), we have $s_\theta=\Delta T/R$. We estimate s_θ from the measured onset at $\Delta T=\Delta T_{c0}$ of Rayleigh convection where $R\simeq 1708$. Even though there is no bifurcation at that point, this onset is well defined by Nusselt number measurements like those presented below in Sec. VI A and Fig. 12. The ratio β_1/β_2 can be taken from independent measurements [34]. Over the range of interest here, it is to a very good approximation independent of concentration and equal to 0.003 57 K^{-1}. Values of ΔT_{c0}, s_θ, and s_c for our three cells and for $x=0.292$ at a mean temperature of 27 °C are given in Table III. Over the range of the mean temperatures of our experiments s_θ and s_c may be regarded as constant for our purpose.

In terms of the modes retained in the model, $\theta(\mathbf{x},z)$ and $\zeta(\mathbf{x},z)$ are given by Eqs. (2.4d) and (2.4e) of ML. The shadowgraph signal is determined by the vertical averages $\theta(\mathbf{x})$ and $\zeta(\mathbf{x})$ of these modes. These averages are given by

$$\theta(\mathbf{x})=\frac{4\sqrt{2}}{\pi}[\hat{\theta}_{101}\cos(qx)+\hat{\theta}_{011}\cos(qy)] \tag{4.4}$$

and

$$\zeta(\mathbf{x})=2[\hat{\zeta}_{100}\cos(qx)+\hat{\zeta}_{010}\cos(qy)]\ . \tag{4.5}$$

For a square pattern, we have $\hat{\theta}_{101}=\hat{\theta}_{011}$ and $\hat{\zeta}_{100}=\hat{\zeta}_{010}$ and henceforth we will refer to them with unsubscripted symbols. For their contribution to the vertical average of the refractive index we then have

$$\delta n(\mathbf{x})=\alpha[\cos(qx)+\cos(qy)]\ , \tag{4.6}$$

with

$$\alpha=\frac{4\sqrt{2}}{\pi}(n_{\tilde{\theta}}s_\theta+\Psi n_{\tilde{c}}s_c)\hat{\theta}+2n_{\tilde{c}}s_c\hat{\zeta}\ , \tag{4.7}$$

where

$$n_{\tilde{\theta}}\equiv(\partial n/\partial T)_{P,x} \tag{4.8a}$$

and

$$n_{\tilde{c}}\equiv(\partial n/\partial x)_{P,T}\ . \tag{4.8b}$$

From the measurements by Kolodner, Williams, and Moe [12] (KWM) we have $n_{\tilde{\theta}}=-2.45\times10^{-4}$ K^{-1} and $n_{\tilde{c}}=0.053$ for $x=0.292$ and $T=27$ °C. Over our range of x and T these may be regarded as constant.

The mode amplitudes needed to calculate α have been derived from the ten-mode model of ML only for the case

$$q=q_{c0}=\pi/\sqrt{2}\ ,$$

where q_{c0} is the critical wave number at the onset of convection for $\Psi=0$ and for slip boundary conditions. In that case, they are related to the variables in the model by [Eq. (2.6a) of ML]

$$\hat{\theta}=\frac{R_{c0}}{\tilde{q}}Y_1 \tag{4.9a}$$

and

$$\hat{\zeta}=\frac{2\sqrt{2}R_{c0}}{\pi\tilde{q}}U_1\ , \tag{4.9b}$$

with

$$R_{c0}=\frac{\tilde{q}^{\,6}}{q_{c0}^2} \tag{4.9c}$$

and

$$\tilde{q}^{\,2}=q_{c0}^2+\pi^2\ . \tag{4.9d}$$

The stationary solutions of the model that correspond to a square pattern are given by [Eq. (3.2g) of ML]

$$Y_1=r\frac{1+4X_1^2/(3\eta)}{1+[2-25\sigma b/(9\eta)]X_1^2}X_1 \tag{4.10a}$$

and

$$U_1=\Psi\frac{\mathcal{L}/2-8X_1^2/3}{\mathcal{L}^2/6+2X_1^2}Y_1\ . \tag{4.10b}$$

Here X_1 is given by the positive root of the cubic equation in X_1^2 [Eq. (3.2b) of ML]

$$X_1^6+a_2X_1^4+a_1X_1^2+a_0=0\ . \tag{4.10c}$$

We do not reproduce the coefficients a_i because they are somewhat complicated, but they are given explicitly by Eqs. (3.2c)–(3.2e) of ML. To evaluate Eqs. (4.10), we also need

$$\eta=\sigma\left[r(1+\Psi)-\frac{500}{27}\right] \tag{4.11a}$$

and

$$b=4\pi^2/\tilde{q}^{\,2}\ . \tag{4.11b}$$

For our mixtures, a representative value of the Prandtl number is $\sigma\simeq 21.6$. We have now summarized all the information necessary to calculate the experimentally measurable refractive-index variation $\delta n(\mathbf{x},r)$ and to compare the variance of $\nabla^2\delta n(\mathbf{x})$

$$P=\alpha^2q^4 \tag{4.12}$$

with the experimental measurement of (P_1+P_2) or of P_r.

The other measurable quantity that is predicted by the model is the Nusselt number $\mathcal{N}$. It is given by

$$\mathcal{N}-1=S_1Z/r\ . \tag{4.13a}$$

Here $S_1=2$ for slip boundary conditions. For squares, Z is given by

$$Z=2X_1Y_1\ . \tag{4.13b}$$

For nonslip boundary conditions, S_1 depends upon σ and for our mixtures should be [46] near 1.4. However, in the physical system it is known to depend on the lateral extent of the sample cell [33] and it is best determined from a fit to the data at a relatively large value of r where, however, the flow pattern still consists of squares. The measurements given in Sec. VI A yield $S_1=1.30$, in remarkably good agreement with the theory [46].

B. Prediction for the refractive index

There are two contributions to the refractive-index variation. One comes from the temperature field θ and the other from the concentration field $c=\zeta+\Psi\theta$. In order to see the relative sizes of the contributions, we consider the case of a square pattern and write

$$\theta=\hat{\theta}_0[\cos(qx)+\cos(qy)] \tag{4.14}$$

and

$$c=\hat{c}_0[\cos(qx)+\cos(qy)]\ . \tag{4.15}$$

Then

$$\hat{\theta}_0=(4\sqrt{2}/\pi)\hat{\theta} \tag{4.16}$$

and

$$\hat{c}_0=2\hat{\zeta}+(4\sqrt{2}/\pi)\Psi\hat{\theta}\ . \tag{4.17}$$

The amplitudes $\hat{c}_0$ and $\hat{\theta}_0$ are plotted in Fig. 5 as a function of r for the particular set of parameters $\Psi=0.0073$, $\mathcal{L}=0.0071$, and $\sigma=21.6$, which is typical of the experiments. At this level, where the fields are still dimensionless, both seem to be about equally important for $r\lesssim 0.75$. In this range, $c\simeq\zeta$ since Ψ is small. At larger r, the temperature mode dominates.

In order to see the actual contributions to the refractive index, we computed the physical amplitudes

$$\hat{n}_\theta=n_{\hat{\theta}}s_\theta\hat{\theta}_0 \tag{4.18}$$

and

$$\hat{n}_c=n_cs_c\hat{c}_0\ , \tag{4.19}$$

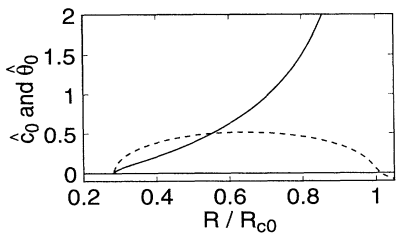

FIG. 5. Amplitudes $\hat{\theta}_0$ (solid line) and $\hat{c}_0$ (dashed line) of the two dimensionless fields that contribute to the refractive-index variation. The example is for $\Psi=0.0073$, $\mathcal{L}=0.0071$, and $\sigma=21.6$.

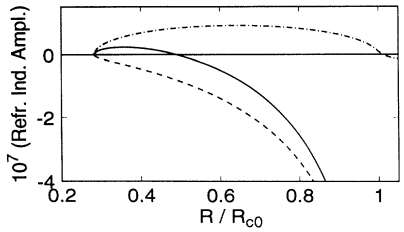

FIG. 6. Contributions $\hat{n}_\theta$ (dashed line) and $\hat{n}_c$ (dash-dotted line) to the refractive-index amplitude of cell 1 for $\Psi=0.0073$, $\mathcal{L}=0.0071$, and $\sigma=21.6$. The solid line is their sum and gives the total refractive-index amplitude.

which yield the refractive-index field

$$\delta n(\mathbf{x})=(\hat{n}_\theta+\hat{n}_c)[\cos(qx)+\cos(qy)] . \tag{4.20}$$

Note that $\hat{n}_\theta+\hat{n}_c=\alpha$ with α given by Eq. (4.7). The amplitudes $\hat{n}_\theta$ and $\hat{n}_c$ are shown in Fig. 6 as dashed and dash-dotted lines. Since $n_{\bar{\theta}}$ (and thus $\hat{n}_\theta$) is negative and $n_{\bar{c}}$ is positive and since the temperature and concentration fields are in phase when $\psi>0$, we see that the two fields contribute with opposite signs and similar magnitudes when R is small. Thus the actual signal visible in the experiment is the relatively small sum of the two contributions of opposite sign, which is shown as a solid line in Fig. 6. As R approaches R_{c0}, the temperature field dominates. At small r, the model predicts that the shadowgraph signal should vanish at a value of r above r_c where the two contributions have the same magnitude.

V. RESULTS AT NEGATIVE Ψ

The measurements of Ψ as a function of x by Kolodner, Williams, and Moe [12] cover a wide range of parameters and for Ψ not too close to zero are definitive. However, the present work is for Ψ very close to zero where the physical phenomena vary extremely rapidly with Ψ. For the interpretation of our data it is necessary to know $\Psi(x)$ with greater precision than can reasonably be obtained from measurements by conventional techniques [12]. Thus we used a measurement of one of the physical properties, which varies rapidly with Ψ near $\Psi=0$ and is predicted accurately by theory to provide a calibration of the relationship between Ψ and x in the range of interest. Specifically, we measured the Hopf frequency over a range of concentrations for Ψ just below zero and from it and the prediction [18–20,22,47] inferred $\Psi(x)$. The data are readily extrapolated to the slightly positive values of Ψ, which are of interest in the rest of this work.

Figure 7 shows shadowgraph images for $x=0.286$ and cell 2 ($d=0.240$ cm). They were taken at the times (in units of $t_v=57$ s) indicated in each figure after $\epsilon\equiv\Delta T/\Delta T_c-1$ was raised from -0.001 to $+0.001$. From the early images it can be seen that the pattern

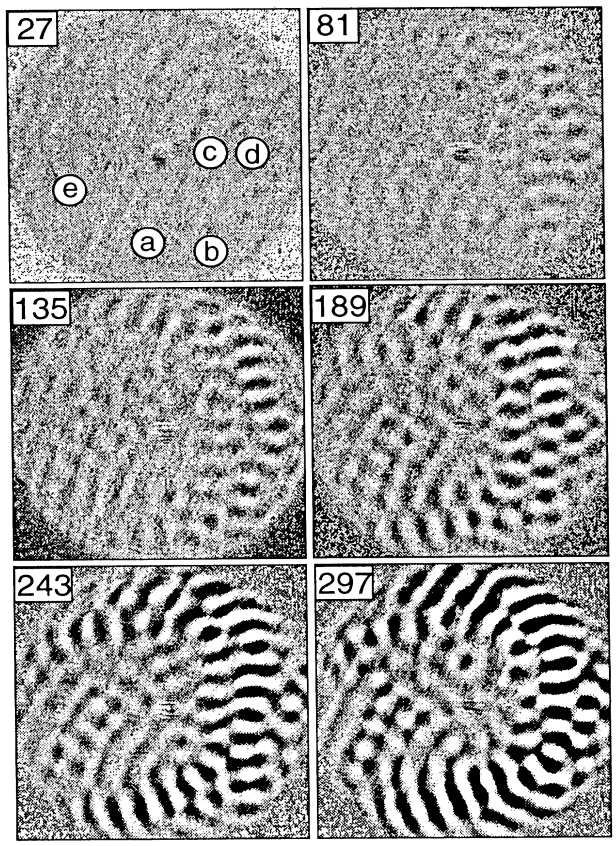

FIG. 7. Shadowgraph images during the transient leading to traveling-wave convection for negative Ψ after ϵ was raised from -0.001 to $+0.001$. This run is for $x=0.286$, cell 2 with $d=0.240$ cm, and $\bar{T}=28.3$ °C ($\Psi=-0.0037$). The number in each image corresponds to the time, in units of t_v, that elapsed since ϵ was raised. Time series of the signal were taken at the locations shown in the top left image.

grows spontaneously, presumably from fluctuations [33], in the sample interior and that its growth is not initiated, for instance, by forcing due to the sidewall or other inhomogeneities [32,33,48,49]. Although not evident from the images, the patterns that formed consisted of traveling convection rolls. As can be seen, they were spatially disorganized. In the top left image, five locations labeled $a-e$ are identified at which time series of the shadowgraph intensity were acquired. These time series are shown in Fig. 8 (each time sequence was scaled differently so that all of them might be shown in the figure with comparable amplitudes). At each location, the signal was oscillatory and had an amplitude that grew in time. Fitting the data over time intervals corresponding to about three periods to the function

$$I=I_0+I_1\sin(\omega t+\phi)\exp(st)$$

yielded values of ω as a function of time. At early times, when the amplitudes were small, all five locations gave the same result for ω. The data for locations a and c are shown in Fig. 9. They show that, for times less than

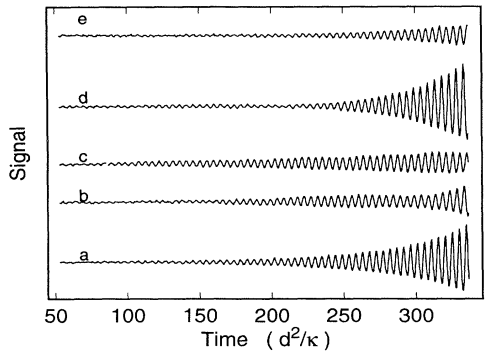

FIG. 8. Shadowgraph signals corresponding to the five locations shown in the top left image of Fig. 7. Each signal is scaled differently so that they all become discernable in the same figure.

about $300t_v$, ω is independent of time and thus of signal amplitude. For larger times, nonlinear effects influence ω and, as expected from measurements at more negative Ψ, ω decreases with increasing amplitude. The early time results determine the Hopf (i.e., linear) frequency within better than 1%. For the particular case shown in Figs. 7–9, the result was $\omega=1.33$ as shown by the horizontal line in Fig. 9.

Figure 10 shows the theoretical result [18–20,22,47] for ω as a function of Ψ. Having determined ω from the experiment, it is a simple matter to determine Ψ from this curve. The results for $\Psi(x)$ corresponding to the four concentrations $x=0.287$, 0.286, 0.284, and 0.280 at a mean temperature $\bar{T}=28.3\,^{\circ}\mathrm{C}$ are shown in Fig. 11(a) as solid circles. Also shown are the results at 30 °C of KWM. The solid and dashed curves are Eq. (10) of KWM, evaluated for 28 °C and 30 °C, respectively. The temperature dependence suggested by these two lines is slight and clearly there is good overall agreement between the two sets of measurements.

Figure 11(b) gives an expanded view of the range of the new data. Here the solid and open symbols are our results for $T=28.3\,^{\circ}\mathrm{C}$ and 32.3 °C, respectively. For reference, we show as a dash-dotted line the relationship given

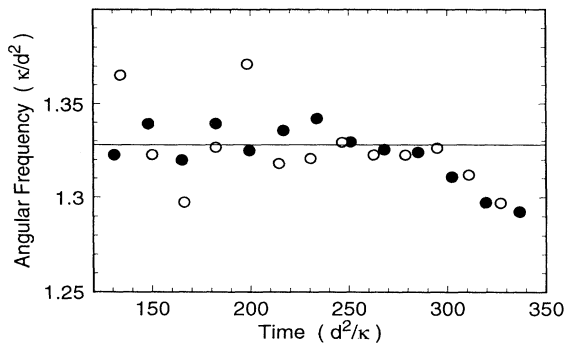

FIG. 9. Dimensionless frequency ω as a function of time measured at locations (a) (solid circles) and (e) (open circles) of Fig. 7. The mass fraction was $x=0.286$.

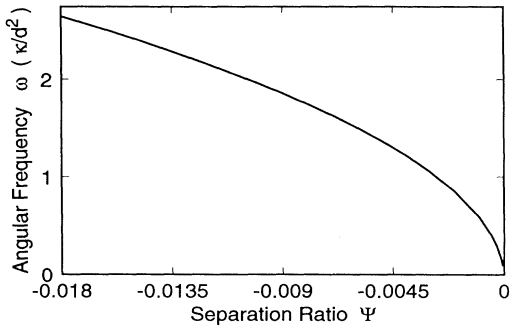

FIG. 10. Dependence of ω upon Ψ for Ψ below but close to zero.

by Eq. (10) of KWM for 28 °C. We fit the new data to a linear dependence of Ψ upon x and obtained

$$\Psi=-0.5165+1.793x \tag{5.1a}$$

for $\bar{T}=28.3\,^{\circ}\mathrm{C}$ and

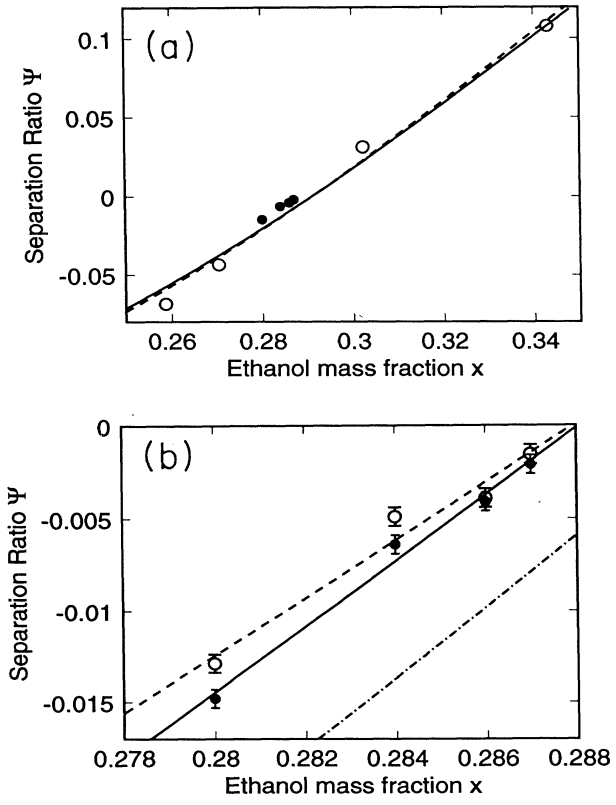

FIG. 11. (a) Separation ratio Ψ as a function of the ethanol mass concentration x over a relatively wide range of Ψ. Open circles, results from Ref. [12] at 30 °C; solid circles, this work at 28.3 °C. The solid and dashed lines correspond to Eq. (10) of Ref. [12], evaluated at 30 °C and 28 °C, respectively. (b) Separation ratio Ψ as a function of the ethanol mass concentration x for $\Psi<0$. Open circles, experimental data for $T=32.3\,^{\circ}\mathrm{C}$; solid circles, experimental data for $T=28.3\,^{\circ}\mathrm{C}$; dashed line, fit to the data at 32.3 °C; solid line, fit to the data at 28.3 °C; dash-dotted line, Eq. (10) of Ref. [12] evaluated for $T=28\,^{\circ}\mathrm{C}$.

$$\Psi = -0.4525 + 1.571x \tag{5.1b}$$

for $\bar{T} = 32.3\,^{\circ}\mathrm{C}$. These fits are shown by the solid and dashed lines, respectively, in Fig. 11(b). We used these results to obtain two values of Ψ for each of the mixture concentrations that we used in the experiments. We then linearly interpolated between these two values to get the value of Ψ at the mean temperature of a particular experiment. The results of this procedure led to the values of Ψ quoted in Table I.

On the scale of Fig. 11(b), there is a significant difference between the new and the old data. In particular, the value of x at which Ψ passes through zero differs by about 0.004. This difference is crucial in the interpretation of our results for positive Ψ. It can also be seen that the fits to the data for the two temperatures pass through zero at the *same* concentration, namely, at $x = 0.288\,06$ and $0.288\,03$. Including possible systematic errors in our concentrations, we find that Ψ vanishes for

$$x_0 = 0.2880 \pm 0.0005\ , \tag{5.2}$$

effectively independent of temperature over the rather narrow temperature range of our experiments. This fact, and the rather small temperature dependence for $\Psi < 0$, indicates that non-Boussinesq effects [50] are relatively unimportant in these mixtures and do not become of overwhelming importance as Ψ goes through zero.

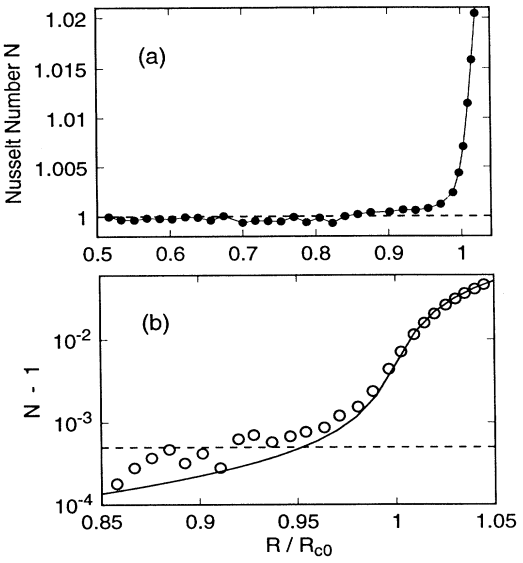

FIG. 12. Nusselt-number measurements for cell 1 and $x = 0.292$ ($\Psi = 0.0073$). (a) $\mathcal{N}$ on linear scales; (b) the convective contribution $\mathcal{N} - 1$ on a logarithmic scale. The solid line in (b) is the prediction of the ten-mode model [Eq. (4.13)], with S_1 in Eq. (4.13a) adjusted to fit the data near $R/R_{c0} = 1$. The dashed horizontal line gives an indication of the size of possible systematic errors in $\mathcal{N}$.

VI. RESULTS AT POSITIVE Ψ

A. Results for the Nusselt number

Figure 12(a) shows results for the Nusselt number for $x = 0.292$ and $T = 26.44\,^{\circ}\mathrm{C}$ ($\Psi = 0.0073$, $\mathcal{L} = 0.007$, and $\sigma = 21.6$, cell 1) on linear scales. The onset of Soret convection in this case is near $r = 0.4$, but $\mathcal{N}$ shows a significant contribution to the heat flux only in the immediate neighborhood of $r = 1$. In Fig. 12(b) we show the convective contribution $\mathcal{N} - 1$ on a logarithmic scale as a function of r. Here the solid line is the prediction Eq. (4.13) of the ten-mode model of ML, with $S_1 = 1.30$ adjusted to fit the data near $r = 1$. The agreement is really better than might be expected. For instance, close inspection of Fig. 12(a) near $r \simeq 0.7$ (where $\mathcal{N}$ is essentially equal to one) suggests that systematic errors as large as 5×10^{-4} can occur in the experiment. This level of uncertainty is indicated in Fig. 12(b) by the horizontal dashed line. It is apparent that nothing can be learned about the behavior of the system near the primary bifurcation (in this case near $r = 0.4$) from a study of $\mathcal{N}$. This is entirely consistent with earlier heat-flux measurements [13,16] at positive Ψ. Nonetheless, the good agreement between the model and the data displayed in Fig. 12(b) is noteworthy.

B. Results for the shadowgraph intensity

Much more can be learned from the shadowgraph images. Figure 13 shows very-high-resolution images from cell 1 for $x = 0.292$ ($\Psi = 0.0073$) at the values of r indicated in the upper right corner of each image. They are representative of many more images and a number of runs in different cells and at different values of Ψ. Typically, r was stepped in increments of 0.01 from below onset and at each value of r the system was allowed to equilibrate for $70t_v$ ($t_v = 107$ s), or about 2 h. Thus a typical run covering the range from $r \simeq 0.3$ to 1.1 took about 1 week. Even though the time scales for pattern evolution are very long, the results are to a reasonable approximation quasistatic. In Fig. 13 it is found that for $r = 0.523$, no pattern is visually discernable. However, at $r = 0.613$, a signal is becoming visible. It is evident that the initial pattern (say, for $r = 0.613$ and 0.700) reaches a significant amplitude over a large portion of the cell interior, demonstrating that there is no noticeable sidewall forcing. Over the entire range of r where a pattern can be observed, the center of the cell shows a square pattern. Along the periphery, the pattern is somewhat disordered and apparently there is some influence of the sidewall on the spatial variation since the rolls are seen to have their axes perpendicular to the wall. However, this influence is different from the usual sidewall inhomogeneity [32,33,48,49], which takes the form of thermal forcing and leads to rolls that have their axes parallel to the wall. The time scale for pattern evolution was too long in this parameter range to wait for further evolution of the patterns and we thus do not know whether in time they would have healed to perfect squares or whether the boundary conditions at the cell wall would have enforced rolls perpendicular to the wall.

In the Rayleigh regime ($r \gtrsim 1$) the sidewall influence was soon overwhelmed by the tendency of the system to

form well-organized rolls. This is shown in Fig. 14. In the range $1.02 \lesssim r \lesssim 1.05$, the pattern became periodically time dependent, as reported by others [14–16]. Beyond that range, one of the sets of rolls became dominant, as shown by the example for $r=1.074$ in Fig. 14. When r was lowered again, the time-periodic regime was encountered again (see $r=1.031$ in Fig. 14), until near $r=1.02$ the pattern was once more one of squares, but now without significant disorder near the sidewalls. As r was decreased further, nearly perfect squares continued to fill the entire cell.

The run of Fig. 14 is continued in Fig. 15, but the contrast of the images is enhanced so that the more feeble patterns can be seen. The squares clearly persist down to $r \simeq 0.61$ and can just barely be seen for $r=0.52$.

More quantitative information about the pattern amplitudes and wave numbers can be obtained by the Fourier-transform techniques described in Sec. III A. Using those methods, the total refractive-index powers $P=P_1^{(3)}+P_2^{(3)}$ and the wave numbers of the patterns (see Sec. III) were determined as a function of r. In Fig. 16 we show the results for the wave numbers for cells 1

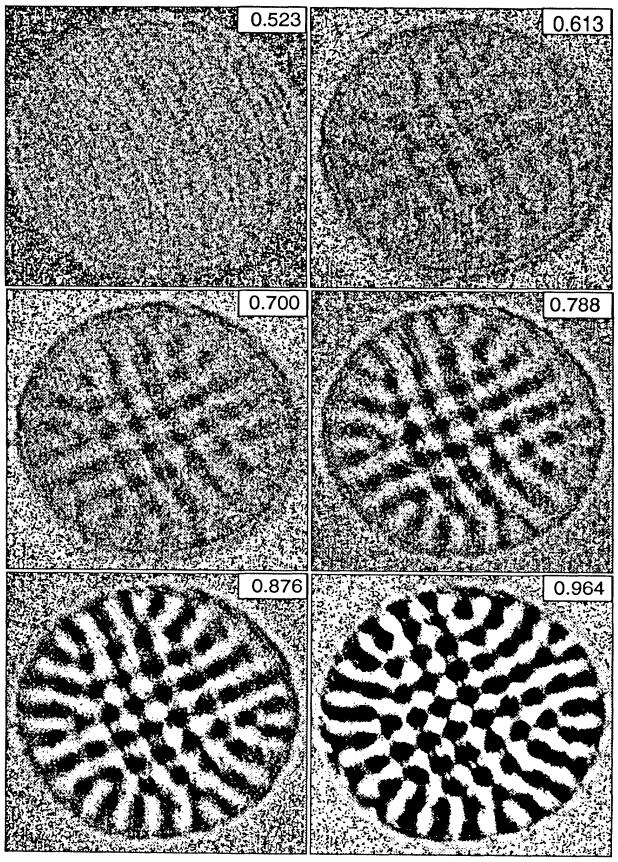

FIG. 13. Some of the shadowgraph images for a run with $x=0.292$ ($\psi=0.0073$) in cell 1. The value of r is given in the upper right corner of each image. The data were taken with increasing r. The steps in r were 0.01, and at each step the pattern was permitted to equilibrate for about 2 h.

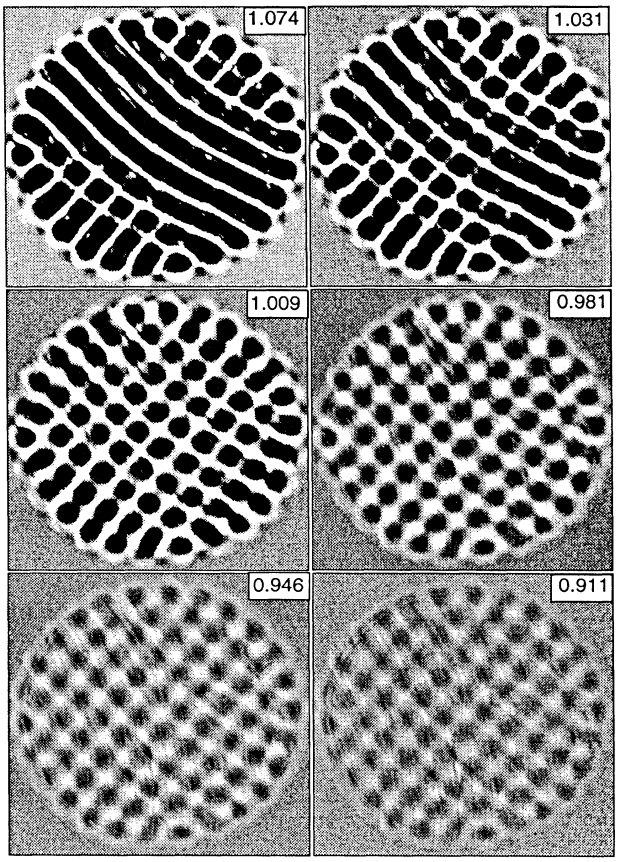

FIG. 14. Continuation of the run illustrated in Fig. 13. After the point corresponding to the upper left image, r was decreased in small steps.

(open circles) and 2 (solid circles), both for $x=0.292$ ($\Psi=0.0073$, $\mathcal{L}=0.007$, $\sigma=21.6$). Also shown are the neutral curves for rigid, impermeable boundary conditions, for $\Psi=0.0073$ (solid curve) and for $\Psi=0$ (dashed curve). We note that above onset there is no theoretical prediction for q and the value chosen by the system is an unsolved wave-number-selection problem. For r close to one, we found that the wave numbers in the experiment were close to those of a pure fluid. As r was decreased, q decreased and tended toward the critical wave number $q_c(\Psi)$ for the mixture. The data for the two cells agree well, except for $r \lesssim 0.6$. In that range close to onset, the very shallow neutral curve for $\Psi=0.0073$ suggests that wave-number-selection processes (which determine q for $r > r_c$) are not very strong and that time constants for pattern adjustments may be extremely long. Thus, in that range the data for the thinner cell 2 (which has a shorter intrinsic time scale t_v) are more likely to represent the true steady state. In any event, it is gratifying that the experimental data generally tend toward $q_c(\Psi=0.0073)=2.1$ as r tends toward r_c.

The refractive-index power for three different runs is shown in Fig. 17. In order to obtain those data from the images, the shadowgraph sensitivity $\mathcal{A}q^2$ [see Eq. (3.5)]

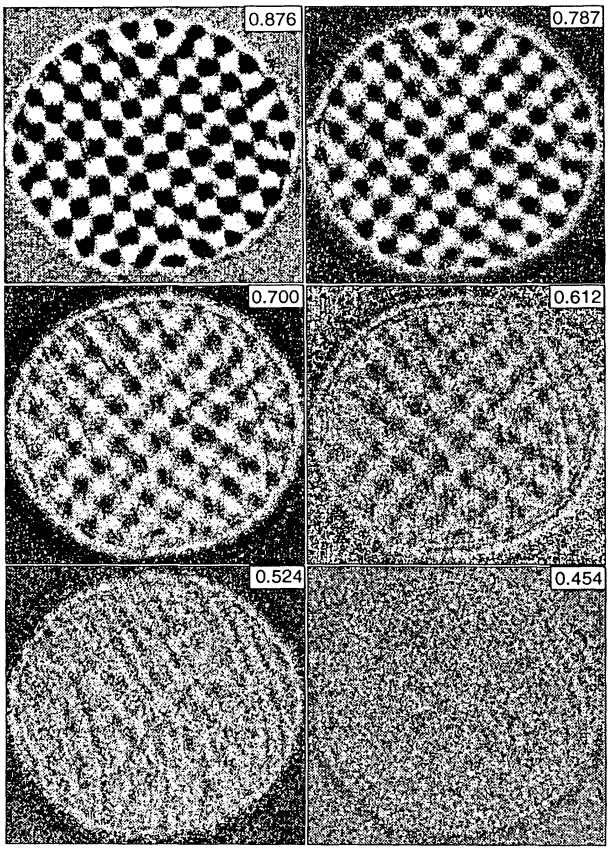

FIG. 15. Continuation of the run in Figs. 13 and 14. Here the images are displayed with greater contrast than in Fig. 14.

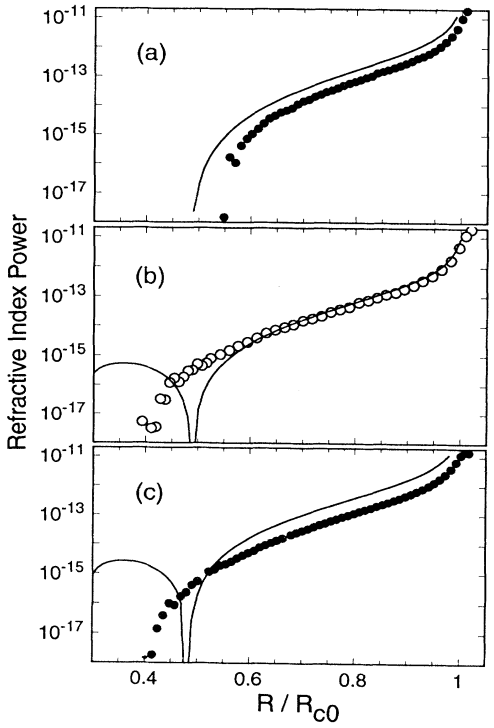

FIG. 17. Refractive-index power as a function of $r=R/R_{c0}$. (a) $x=0.290$, $\Psi=0.0035$, cell 2; (b) $x=0.292$, $\Psi=0.0073$, cell 1 (images for this run are given in Figs. 13–15); (c) $x=0.292$, $\Psi=0.0072$, cell 2. The lines are the predictions of the ten-mode model.

was computed from the measured wave vectors q such as those given in Fig. 16. The solid lines are the predictions of the ten-mode model discussed in Sec. IV. Figure 17(a) is for $\Psi=0.0035$ and cell 2. For this Ψ, the complete cancellation in the model between the contributions from the concentration and the temperature field (see Fig. 6) occurs near $r=0.48$ and the power below that point is outside the vertical range of the figure. In the model, the onset is at $r_c=0.454$, whereas the data give $r_c=0.55$ (see Table I). The experimental onset agrees well with the prediction for the physically realistic impermeable, nonslip boundary conditions, as will be shown below in Fig. 19. For $r>r_c$ the data fall slightly below the model prediction, consistent with the difference in r_c due to the different boundary conditions.

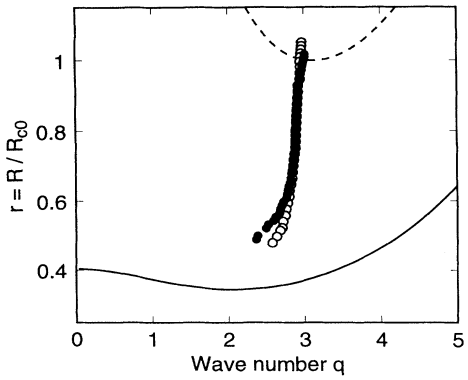

FIG. 16. Selected wave numbers for cell 1 (open circles) and cell 2 (solid circles). The data are for $x=0.292$ ($\Psi=0.0073$, $\mathcal{L}=0.007$, and $\sigma=21.6$). The solid and dashed lines are the neutral curves for $\Psi=0.0073$ and 0, respectively.

Figure 17(b) is for $\Psi=0.0073$ ($x=0.292$) for the run in cell 1 and Fig. 17(c) is for $\Psi=0.0072$ ($x=0.292$) for the run in cell 2. We find $r_c=0.42$ in both cells, whereas the model gives $r_c=0.285$. In this case the figure exhibits more clearly the total cancellation between the concentration and temperature contributions in the model near $r=0.48$ because the model predicts a power below that point which is within the vertical range of the figure. The data do not show this effect and instead vanish monotonically very close to the onset predicted on the basis of nonslip boundary conditions (see Fig. 19 below). We expect that the cancellation in the model is an artifact that would disappear if realistic boundary conditions were used. For cell 2 [Fig. 17(c)] the data in the range $0.5 \lesssim r \lesssim 1$ are again somewhat below the model prediction, consistent with the different onsets. For cell 1 [Fig. 17(b)], the data seem to agree better with the model, but we believe that this is illusory. For this thicker cell, equilibration times were longer and we believe that the

cell-2 data are more likely to correspond to a fully equilibrated steady state. The overall agreement between the data and the model predictions is really very satisfying for all three runs displayed in the figure.

Near onset one would expect all mode amplitudes to grow in proportion to $\epsilon^{1/2}$, where $\epsilon=r/r_c-1$. Thus the refractive-index power should be given by $P=S_1^P\epsilon$ when ϵ is small enough. This behavior is not made obvious with the logarithmic vertical scale of Fig. 17. Thus we show the power on linear scales in Fig. 18. Since the data vary over many orders of magnitude, they are plotted five times, with the vertical scale differing by a factor of 10 each time. All representations except the most expanded plot show strong curvature. However, the greatest data expansion shows that the data nearest r_c are consistent with a linear relationship and a finite initial slope S_1^P. Roughly, we find $S_1^P\simeq 3\times 10^{-14}$ for $\Psi=0.0035$ and $S_1^P\simeq 5\times 10^{-15}$ for $\Psi=0.0073$. However, since these results are based on the few data points that are closest to the limit of resolution and since they are sensitive to the precise background correction that is applied, we regard them to be indicative only roughly of the size of the initial slope. From the ten-mode model, we find the values $S_1^P=4.5\times 10^{-16}$ for $\Psi=0.0035$ and $S_1^P=2.4\times 10^{-14}$ for $\Psi=0.0072$. We do not expect these values to be realistic since they are sensitive to the precise cancellation between the contributions from the temperature and the concentration modes, but find it encouraging to see that they are within a couple of orders of magnitude of the experiment. For comparison, the initial slope for the pure fluid is near 10^{-8}, i.e., six orders of magnitude larger than the measured values. It would be interesting to carry out a weakly nonlinear calculation of S_1^P with realistic boundary conditions. This could be done by the methods used in Refs. [21] and [22], but in practice these papers did not focus on this particular experimentally accessible parameter and do not report the information necessary for the calculation. Finally, it is interesting to note that P is linear in ϵ only for $\epsilon\lesssim 0.1$, as one might have expected.

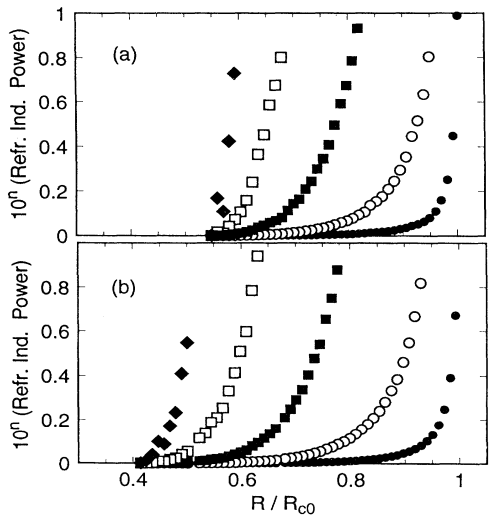

FIG. 18. Refractive-index power P as a function of $r=R/R_{c0}$ on linear scales for cell 2 and (a) $\Psi=0.0035$ and (b) $\Psi=0.0072$. In each plot, the data are shown five times on vertical scales differing by factors of 10. The power was multiplied by 10^n, with $n=11$ (solid circles), $n=12$ (open circles), $n=13$ (solid squares), $n=14$ (open squares), and $n=15$ (solid diamonds).

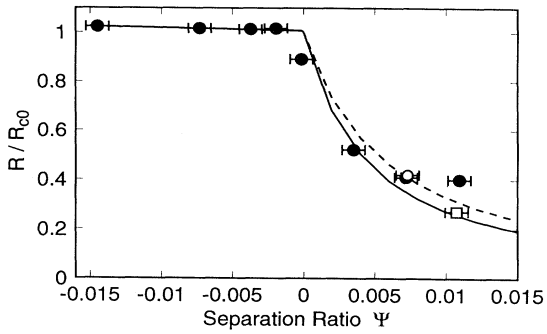

FIG. 19. Experimental (symbols) and theoretical (lines) values of the reduced critical Rayleigh number R_c/R_{c0}. Open circle, cell 1; solid circles; cell 2; open square, cell 3. For $\Psi>0$, the solid (dashed) line is for $\mathcal{L}=0.007$ (0.009). The Prandtl number is $\sigma=21.6$.

The values of $r_c(\Psi)$ determined from data like those shown in Figs. 17 and 18 are given in Fig. 19. There we also show the results for $\Psi<0$ discussed in Sec. V. The lines are the predictions [18–20,22,47] of linear stability analysis for rigid, impermeable boundaries. Since the Lewis number is not known very accurately for these mixtures, the theoretical result for positive Ψ is given for $\mathcal{L}=0.009$ (dashed line) as well as for $\mathcal{L}=0.007$ (solid line). Clearly the overall agreement between theory and experiment is very satisfying.

VII. SUMMARY

We have presented the results of extremely sensitive measurements on convection in binary mixtures with values of the separation ratio Ψ close to zero. For all of our work, the Lewis number $\mathcal{L}$ was close to 0.007 and the Prandtl number σ was near 20. The apparatus used for this purpose is described in some detail in Sec. II. Both Nusselt-number measurements and shadowgraph flow visualizations of convection patterns were done. The Nusselt-number measurements had a resolution of 0.05%. In Sec. III we describe the quantitative shadowgraph method, which enabled us to determine the vertical average of the amplitude of the refractive-index field. The method had the resolution to detect sinusoidal variations in the refractive index with an amplitude of one part in 10^9.

The Hopf frequency ω was measured as a function of concentration x for Ψ below but close to zero. By comparing the experimental frequency with the prediction [18–20,22] $\omega(\Psi)$ of linear stability analysis, the relation between Ψ and x was determined. It could be readily ex-

trapolated to the small values of $\Psi > 0$, which are of interest in the present paper. These results are summarized by Eqs. (5.1).

In order to facilitate a comparison of our shadowgraph measurements at positive Ψ with the ten-mode Galerkin truncation [45] of ML, we wrote down explicitly the relationship between the scaled mode amplitudes Y and U of the model and the amplitude of the refractive-index variation δn, which is determined in the experiment. This is done in Sec. IV. It turns out that the temperature and the concentration variations contribute to δn, and thus to the shadowgraph signal, with opposite signs. Over most of the range $R_c < R \lesssim R_{c0}$, this leads only to a partial cancellation and some signal remains in the experiment. However, according to the model there is complete cancellation at a particular value of $R > R_c$, which for $\Psi = 0.0073$ is near $0.5R_{c0}$. This phenomenon is not observed in the experiment and it is interesting to enquire whether it may be a consequence of the unrealistic slip boundary conditions that had been used in the theory.

At positive Ψ, we made high-resolution measurements of the Nusselt number $n(R)$. As expected from theory and on the basis of previous experiments [13,14,16], these data revealed information about the system only quite close to the Rayleigh onset at $R_{c0} \simeq 1708$ even though the primary bifurcation was at $R_c(\Psi) \simeq 0.4R_{c0}$ for the value $\Psi = 0.0073$ used in the experiment. The Nusselt number gave the appearance of a slightly rounded, i.e., imperfect, bifurcation at R_{c0} and was within the experimental resolution of 5×10^{-4} equal to unity for $R < 0.9R_{c0}$. Nonetheless, it is noteworthy that $n(R)$ agreed well in the rounded region with the prediction of the model of ML.

The most important results of this paper are measurements of the shadowgraph patterns and intensities for $0 < \Psi \leq 0.011$. We were able to visualize the flow patterns and to measure the amplitudes of the associated refractive-index variations even in the immediate vicinity of R_c, where the signal is extremely feeble and where previous experiments [14–16] had been unable to visualize the pattern. In agreement with a prediction by Clune and Knobloch [21], we found stable squares close to onset over the range of Ψ covered by our experiments. There was no indication of a range of R close to R_c where rolls are stable, as had been suggested by the stability analysis [45] of the ten-mode model of ML. From the shadowgraph signal we computed the power of the refractive-index variation (i.e., the square of the modulus of the Fourier transform) as a function of R and compared it with predictions based on the ML ten-mode model. The agreement is very satisfactory, especially when it is considered that the measured power varies by about six orders of magnitude as R changes from just above R_c to R_{c0} and that the model is based on unrealistic slip boundary conditions. The data make it possible to determine R_c/R_{c0} with a resolution of approximately 0.05. Within that uncertainty, the bifurcation line $R_c(\Psi)$ is in excellent agreement with the predictions of linear stability analysis based on realistic rigid, impermeable boundary conditions [18–20,22]. An accurate determination of the wave numbers of the patterns could be made only when R/R_{c0} exceeded its critical value by about 0.1. The results were consistent with a wave number starting at $q_c(\Psi)$ for $R = R_c$, but increasing toward the value $q \simeq 3$ characteristic of the pure fluid as R increased toward R_{c0}. In the Rayleigh regime above R_{c0}, we observed the oscillatory pattern associated with the transition from squares to rolls, which has been reported by others [14–16] and is reproduced by ML's ten-mode model, but we did not study this in any detail.

ACKNOWLEDGMENTS

We are very grateful to W. Hort and W. Schöpf for sharing their stability-analysis programs with us and to M. Lücke, St. Hollinger, and E. Knobloch for comments on a draft of this manuscript. This work was supported by the Department of Energy through Grant No. DE-FG03-87ER13738.

[1] For a recent review, see M. C. Cross and P. C. Hohenberg, Rev. Mod. Phys. **65**, 851 (1993).

[2] M. S. Heutmaker and J. P. Gollub, Phys. Rev. A **35**, 242 (1987).

[3] V. Croquette, Contemp. Phys. **30**, 113 (1989).

[4] V. Croquette, Contemp. Phys. **30**, 153 (1989).

[5] E. Bodenschatz, J. de Bruyn, G. Ahlers, and D. S. Cannell, Phys. Rev. Lett. **67**, 3078 (1991).

[6] E. Bodenschatz, D. S. Cannell, J. R. de Bruyn, R. Ecke, Y.-C. Hu, K. Lerman, and G. Ahlers, Physica D **61**, 77 (1992).

[7] Y. Hu, R. Ecke, and G. Ahlers, Phys. Rev. E **48**, 4399 (1993).

[8] S. W. Morris, E. Bodenschatz, D. S. Cannell, and G. Ahlers, Phys. Rev. Lett. **71**, 2026 (1993).

[9] Y. C. Hu, R. Ecke, and G. Ahlers, Phys. Rev. Lett. **72**, 2191 (1994).

[10] M. Assenheimer and V. Steinberg, Nature (London) **367**, 345 (1994).

[11] Following the seminal work of R. W. Walden, P. Kolodner, A. Passner, and C. M. Surko [Phys. Rev. Lett. **53**, 242 (1984)], which clearly established the occurrence of traveling waves in binary-mixture convection with negative separation ratio, many results were reported by several experimental groups. These are too numerous to be listed here, but a recent summary has been given in Ref. [1], pp. 998–1011. The phenomena encountered include traveling waves, localized pulses, periodically and chaotically time-dependent envelopes of the convection rolls, and patterns consisting of squares.

[12] P. Kolodner, H. L. Williams, and C. Moe, J. Chem. Phys. **88**, 6512 (1988).

[13] G. Ahlers and I. Rehberg, Phys. Rev. Lett. **56**, 1373 (1986).
[14] E. Moses and V. Steinberg, Phys. Rev. Lett. **57**, 2018 (1986).
[15] P. Bigazzi, S. Ciliberto, and V. Croquette, J. Phys. (Paris) **51**, 611 (1990).
[16] E. Moses and V. Steinberg, Phys. Rev. A **43**, 707 (1991).
[17] D. Gutkovicz-Krusin, M. A. Collins, and J. Ross, Phys. Fluids **22**, 1443 (1979); **22**, 1451 (1979).
[18] M. C. Cross and K. Kim, Phys. Rev. A **37**, 3909 (1988).
[19] E. Knobloch and D. R. Moore, Phys. Rev. A **37**, 860 (1988).
[20] W. Schöpf and W. Zimmermann, Europhys. Lett. **8**, 41 (1989).
[21] T. Clune and E. Knobloch, Phys. Rev. **44**, 8084 (1991).
[22] W. Schöpf and W. Zimmermann, Phys. Rev. E **47**, 1739 (1993).
[23] St. Hollinger and M. Lücke, Phys. Rev. E **52**, 642 (1995).
[24] E. Knobloch, Phys. Rev. A **40**, 1549 (1989).
[25] P. LeGal, A. Pocheau, and V. Croquette, Phys. Rev. Lett. **54**, 2501 (1985).
[26] M. Bestehorn, Physica D **61**, 59 (1993).
[27] E. M. Sparrow, R. J. Goldstein, and V. R. Jonsson, J. Fluid Mech. **18**, 513 (1964).
[28] F. H. Busse and N. Riahi, J. Fluid Mech. **96**, 243 (1980).
[29] M. R. E. Proctor, J. Fluid Mech. **113**, 469 (1981).
[30] P. LeGal and V. Croquette, Phys. Fluids **31**, 3440 (1988).
[31] G. Ahlers, D. S. Cannell, L. I. Berge, and S. Sakurai, Phys. Rev. E **49**, 545 (1994).
[32] See, for instance, V. Steinberg, G. Ahlers, and D. S. Cannell, Phys. Scr. **32**, 534 (1985).
[33] C. W. Meyer, G. Ahlers, and D. S. Cannell, Phys. Rev. A **44**, 2514 (1991); M. Wu, G. Ahlers, and D. S. Cannell, Phys. Rev. Lett. **75**, 1743 (1995).
[34] *Zahlenwerte and Funktionen aus Naturwissenschaften und Technik,* edited by K. H. Hellwege, Landolt-Börnstein, New Series, Group X, Vol. IV, Pt. 1b (Springer, Berlin, 1977), p. 129.
[35] *The Physico-Chemical Constants of Binary Systems in Concentrated Solutions,* edited by J. Timmermans (Interscience, New York, 1960), Vol. 4, p. 190.
[36] We used a type H-3000-L "Super Bright" LED, manufactured by Stanley Electric, with a current of about 100 mA.
[37] S. Rasenat, G. Hartung, B. L. Winkler, and I. Rehberg, Exp. Fluids **7**, 412 (1989).
[38] S. Trainoff, D. S. Cannell, and G. Ahlers (unpublished).
[39] For details about Fourier transforms, see, for instance, E. Oran Brigham, *The Fast Fourier Transform* (Prentice-Hall, Englewood Cliffs, NJ, 1974).
[40] Q. Ouyang, G. H. Gunaratne, and H. L. Swinney, Chaos **3**, 707 (1993).
[41] G. H. Gunaratne, Q. Ouyang, and H. L. Swinney, Phys. Rev. E **50**, 2802 (1994).
[42] L. I. Berge, G. Ahlers, and D. S. Cannell, Phys. Rev. E **48**, R3236 (1994).
[43] G. Ahlers, in *Pattern Formation in Liquid Crystals,* edited by L. Kramer and A. Buka (Springer, Berlin, 1995).
[44] D. R. Jenkins, J. Fluid Mech. **190**, 451 (1988).
[45] H. W. Müller and M. Lücke, Phys. Rev. A **38**, 2965 (1988).
[46] A. Schlüter, D. Lortz, and F. Busse, J. Fluid Mech. **23**, 129 (1965).
[47] W. Schöpf, Diplom thesis, Universität Bayreuth, 1988 (unpublished).
[48] G. Ahlers, M. C. Cross, P. C. Hohenberg, and S. Safran, J. Fluid Mech. **110**, 297 (1981).
[49] M. C. Cross, P. C. Hohenberg, and M. C. Lücke, J. Fluid Mech. **136**, 169 (1983).
[50] S. J. Linz and M. Lücke, Phys. Rev. A **36**, 3505 (1987).

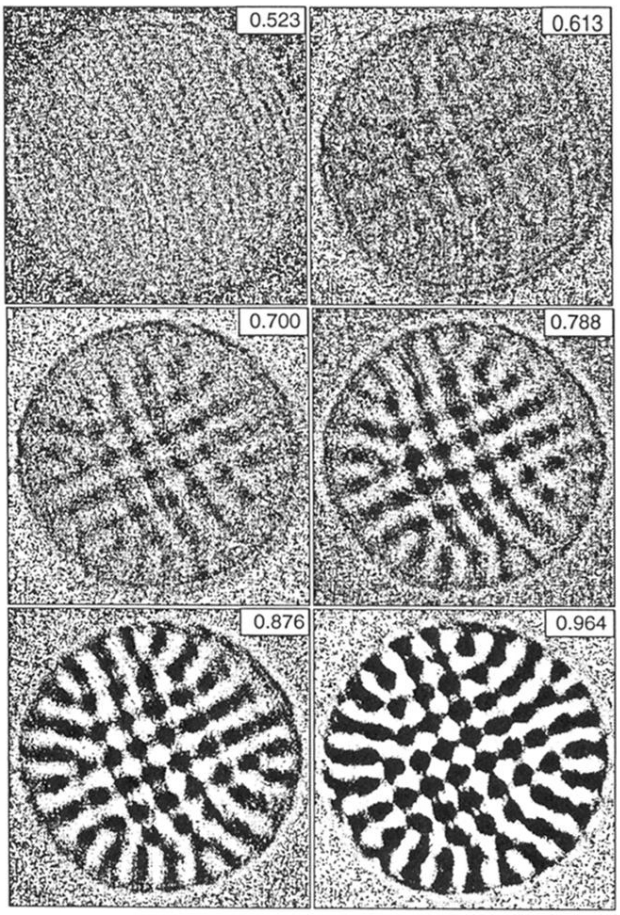

FIG. 13. Some of the shadowgraph images for a run with $x=0.292$ ($\psi=0.0073$) in cell 1. The value of r is given in the upper right corner of each image. The data were taken with increasing r. The steps in r were 0.01, and at each step the pattern was permitted to equilibrate for about 2 h.

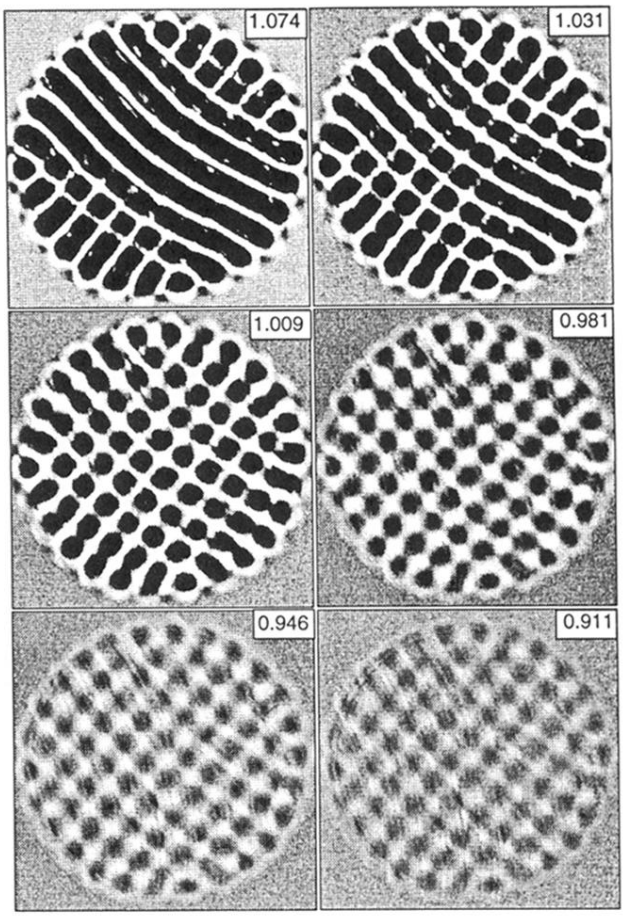

FIG. 14. Continuation of the run illustrated in Fig. 13. After the point corresponding to the upper left image, r was decreased in small steps.

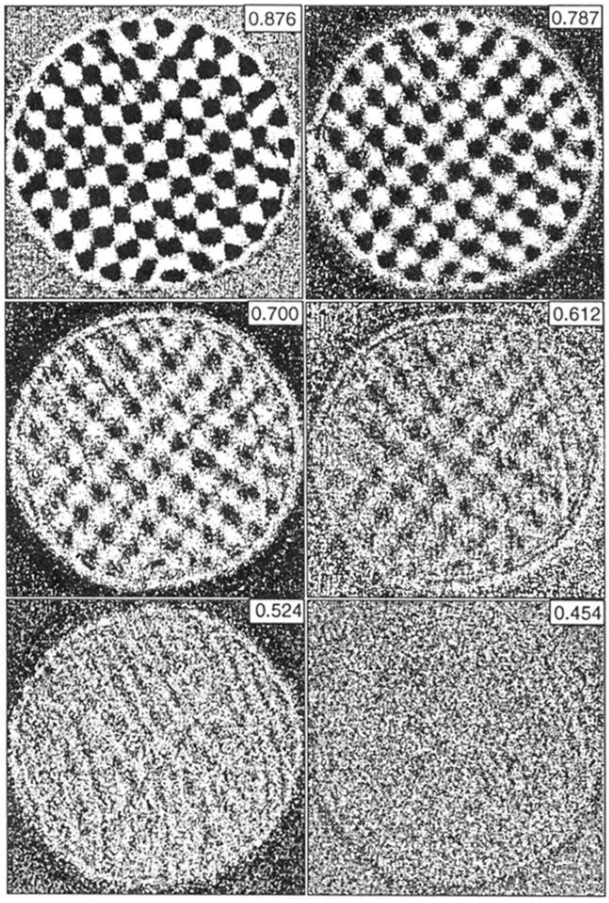

FIG. 15. Continuation of the run in Figs. 13 and 14. Here the images are displayed with greater contrast than in Fig. 14.

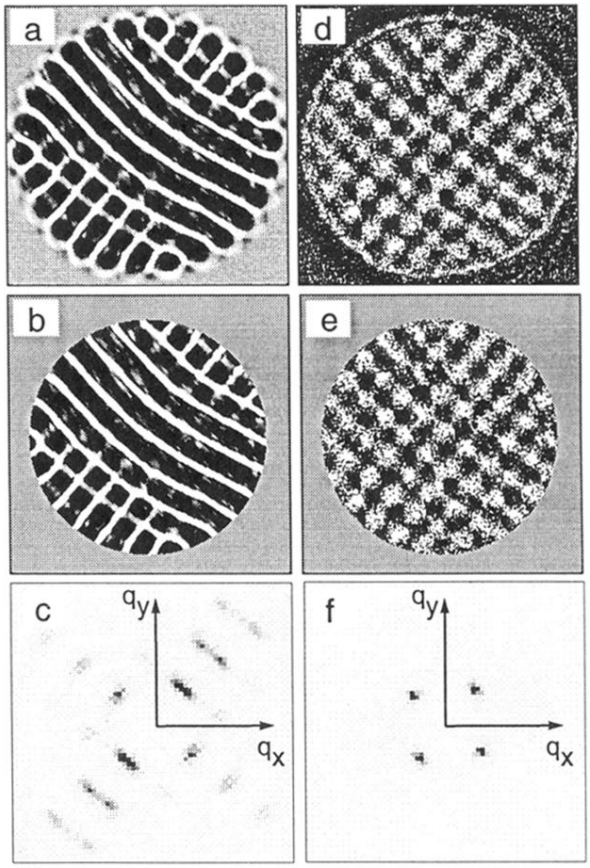

FIG. 3. Gray-scale images of convection patterns from cell 1 for $\Psi=0.0073$ ($x=0.292$). (a) and (d) are images of the entire cell for $r=1.05$ and 0.68, respectively. (b)and (e) are the portions used in the Fourier analysis. (c) and (f) are the corresponding gray-scale representations of the center $\frac{1}{4}\times\frac{1}{4}$ portions of the structure factors of the images in (b) and (e).

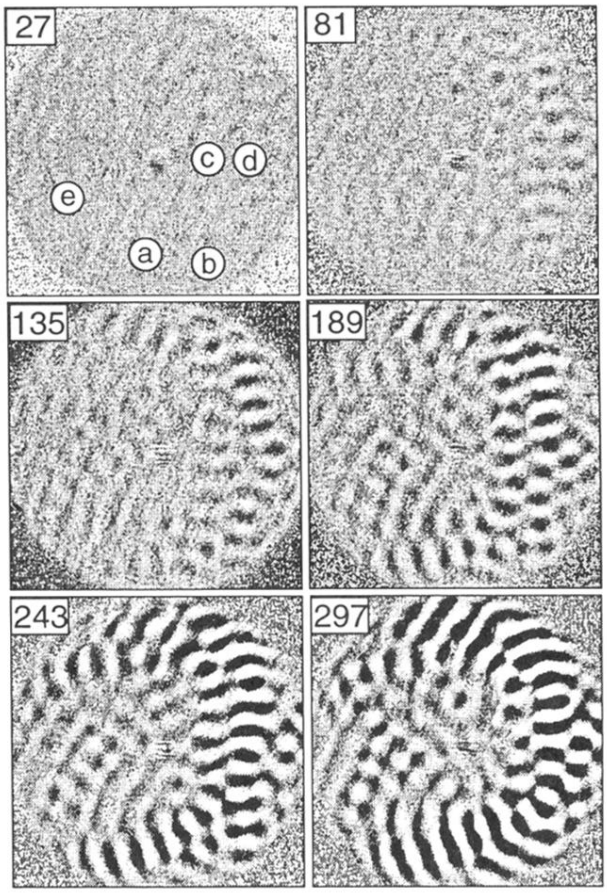

FIG. 7. Shadowgraph images during the transient leading to traveling-wave convection for negative Ψ after ϵ was raised from -0.001 to $+0.001$. This run is for $x=0.286$, cell 2 with $d=0.240$ cm, and $\bar{T}=28.3$°C ($\Psi=-0.0037$). The number in each image corresponds to the time, in units of t_v, that elapsed since ϵ was raised. Time series of the signal were taken at the locations shown in the top left image.